Continuous-time random walk model for the diffusive motion of helicases

V. Rodríguez-Franco[1], M.M. Spiering[2], P. Bianco[3], F. Ritort[1,4,5], M. Mañosas[1,4]

[1] *Small Biosystems Lab, Condensed Matter Physics Department,*
Universitat de Barcelona, Carrer de Martí i Franquès 1, 08028 Barcelona, Spain
[2] *Department of Chemistry, The Pennsylvania State University, University Park, PA, USA*
[3] *Department of Pharmaceutical Sciences, College of Pharmacy,*
University of Nebraska Medical Center, Omaha, Nebraska 68198-6025, USA
[4] *Institut de Nanociència i Nanotecnologia, Universitat de Barcelona, 08029 Barcelona, Spain and*
[5] *Reial Acadèmia de Ciències i Arts de Barcelona (RACAB),*
Secció Física.2a, La Rambla 115, E-08002 Barcelona, Spain

Abstract:

DNA helicases are molecular motors that use the energy from nucleotide hydrolysis to move along DNA, promoting the unwinding or rewinding of the double helix. Here, we use magnetic and optical tweezers to track the motion of three helicases, gp41, RecQ, and RecG, while they unwind or rewind a DNA hairpin. Their activity is characterized by measuring the helicase velocity and diffusivity under different force and ATP conditions. We use a Continuous-Time Random Walk framework that allows us to compute the mean helicase displacement and its fluctuations analytically. Fitting the model to the measured helicase velocity and diffusivity allows us to determine the main states and transitions in the helicase mechanochemical cycle. A general feature for all helicases is the need to incorporate an off-pathway pausing state to reproduce the data, raising the question of whether pauses play a regulatory role. Diffusivity measurements also lead to estimations of the thermodynamic uncertainty factor related to the motor efficiency. Assuming a tight mechano-chemical coupling we find that the RecG helicase reaches a high efficiency when operating uphill, whereas the unwinding gp41 and RecQ helicases display much lower efficiencies. Incorporating the analysis of fluctuations allows to better characterize the activity of molecular machines, which represents an advance in the field.

I. INTRODUCTION

Helicases are ubiquitous enzymes that are present in all living organisms. They work as molecular motors, converting the chemical energy from the hydrolysis of adenosine triphosphate (ATP) into mechanical work and motion along nucleic acids (NA) [1, 2]. Helicase motion is coupled to various functions, such as: NA unwinding and separation of the two strands of the duplex (e.g. in DNA replication and transcription); NA rewinding and formation of multi-branch structures (e.g. in DNA recombination); and disruption of protein-NA interactions (e.g. in DNA repair and RNA processing) [2–4]. These diverse functions are accomplished by the presence of different helicases, classified into families based on their conserved structural motifs [5, 6]. Besides their relevance in molecular biology, helicases, and molecular motors in general, have raised interest in many other fields, and in physics, they are a paradigm of small systems [7]. Molecular motors typically move in nanometer (nm) steps while generating mechanical forces on the picoNewton (pN) range, leading to the generation of work of pN·nm, which is on the order of the thermal energy unit $k_B T$ ($1k_B T = 4$pN·nm). On the other hand, the energy released by the hydrolysis of ATP is $\sim 10 k_B T$, which implies that these motors work on a strong Brownian environment where fluctuations play a central role.

The helicase translocation along the NA strand in a defined directionality (3' to 5' or 5' to 3') results from different nucleotide-enzyme conformations of distinct NA affinities connected in a cyclic reaction network [8, 9].

The mechano-chemical coupling between the ATP hydrolysis reaction and the enzyme motion can be described in terms of two mechanisms: the Brownian Ratchet (BR) and the Power Stroke (PS) [4, 9–12]. These two mechanisms exemplify the two limit cases: biasing or rectifying the motor diffusive thermal motion (BR) versus downhill dynamics based on a motor structural change induced by ATP hydrolysis (PS). In practice, many molecular motors may employ a combination of both mechanisms to achieve efficient motion [11]. These two mechanisms can also be used to describe motor translocation coupled to NA strand separation/rewinding during NA unwinding/rewinding, leading to the classification of helicases as active (for PS) and passive (for BR) [9, 12, 13]. The active helicase directly interacts with the ssNA/dsNA junction, destabilizing (or stabilizing) the base-pairs (bp) at the fork before translocation. In contrast, the passive helicase relies on the thermal fraying of the bp at the NA fork to promote un(re)winding.

Traditionally, helicase activity has been characterized using ensemble assays, such as gel-based or fluorescence spectroscopy [14–16]. These approaches measure average properties over a large ensemble of molecules, but they provide limited information about nanoscale processes where fluctuations are relevant. In the last 30 years, different single molecule techniques have emerged [17, 18], allowing to monitor the activity of individual enzymes in real-time. These measurements facilitate the detection of molecular heterogeneity, rare events, pathways, intermediates, and dynamical NA-helicase interactions [19], crucial aspects for understanding how helicases work. The movement of single helicases can be monitored

using single-molecule force spectroscopy techniques, such as optical, magnetic or nanopore tweezers [17, 20–22]. In these assays, a mechanical force is applied on the enzyme or along the NA substrate, and the NA extension along the force direction is measured, defining a reaction coordinate to follow the advance of the helicase [23]. By modifying the nucleotide conditions (e.g. ATP and ADP concentrations) and the applied force, the coupling between the helicase motion and the ATP hydrolysis reaction can be investigated, discriminating between different helicase mechanisms [13, 24–28]. The general approach has been to use the experimental data to test specific models for each helicase, finding that, in many cases, different helicases display distinct activities involving complex reactions with multiple kinetic pathways and/or different rate-limiting steps.

Most descriptions of molecular motors are based on simple kinetic models and pathways. From muscle transport motors such as kinesin and myosin, to genomic maintenance machines such as polymerases and helicases, most models have focused on describing the average motor velocity under different conditions of ATP, ADP, force and temperature [29–31]. However, a main feature of these machines is the Brownian fluctuations and their diffusivity. Despite its importance, the helicase diffusivity has not been analysed in detail before. The diffusion constant (D), along with the velocity (v), are of particular interest as they are related to the randomness parameter $r = \frac{2D}{dv}$, where d is the motor step-size [32]. This parameter provides information about the number of rate-limiting steps in an enzymatic cycle, being $r = 1$ for a Poisson process and $r = 0$ for a molecular clock. Alternatively, the motor step-size d can be estimated if the number of rate-limiting steps is known [33]. Additionally, v and D are related to the $\mathcal{Q}$ factor of the thermodynamic uncertainty relation (TUR) [34, 35]. The TUR sets an inequality between the entropy production rate σ and the measurement precision in nonequilibrium steady states. It is defined in terms of generic nonequilibrium currents, which for the case of a translocating motor takes the form $\mathcal{Q} = \sigma \frac{2D}{k_B v^2} \geq 2$ with σ expressed in k_B units [35]. This factor quantifies the irreversibility of an enzymatic process in the non-linear regime and is related to the motor's thermodynamic efficiency η defined as the ratio between the amount of delivered mechanical work (W) and the input chemical energy coming from the ATP hydrolysis ($\Delta\mu$): $\eta = \frac{W}{\Delta\mu}$. The two quantities satisfy the energy balance relation, $\Delta\mu = W + T\sigma t$, where T is the temperature and $T\sigma$ stands for the heat rate released to the environment. The thermodynamic efficiency η can be expressed in terms of $\mathcal{Q}$, $\eta = (1 + \mathcal{Q}\frac{vd}{2D}\frac{k_B T}{W})^{-1}$ [35, 36], small $\mathcal{Q}$ values indicating a more efficient motor that operates closer to the limits of thermodynamic optimization.

In this work, we have investigated three different DNA helicases using magnetic tweezers (MT) and optical tweezers (OT). Two of them catalyse DNA unwinding: the T4 gp41 helicase, which is involved in DNA replication in T4 bacteriophage, and RecQ from Escherichia

Coli (*E.coli*), which participates in different DNA repair pathways. The third one is the RecG helicase from *E.coli*, which is involved in DNA repair and recombination, catalysing DNA rewinding and the formation of multi-branched DNA structures [13, 37–42]. In the experiments, a constant force is applied to the extremities of a DNA hairpin, and the helicase un(re)winding activity is followed by measuring the changes in the DNA extension, enabling real-time monitoring of the enzyme activity. From these measurements, we can infer the position of the helicase along the DNA and extract its mean velocity, diffusivity, and pause kinetics. To interpret the experimental results, we have developed a general theoretical framework for helicase motion based on random-walk theory. The model features a continuous-time random walk (CTRW) in a one-dimensional chain with an auxiliary pausing state. There are three distinct kinetic transitions: forward, backward, and enter/exit a pause. Each transition is described by activated kinetic rates that depend on the force and ATP concentration ([ATP]). The model fits the translocation and unwinding/rewinding rates and diffusivity data for the different helicases over a range of forces and [ATP]. The fitting procedure allows us to determine the chemical (ATP concentration) and mechanical (force) dependencies of the kinetic rates connecting the different states, providing insight into the helicase mechano-chemical cycle. Assuming a tight mechano-chemical coupling, we have also investigated how the $\mathcal{Q}$ factor and the motor efficiency η change for each helicase and how their values depend on the helicase step-size and its active and passive nature.

II. METHODS

A. DNA substrates

Two different hairpins, h1.2 and h1.4, of ∼1.2 and ∼1.4 kbp stems respectively, have been used for the MT and OT assays. Both hairpins have a 5' single-stranded DNA (ssDNA) tail of ∼80 nucleotides (nts) labelled with a biotin and 3' ssDNA tail of ∼100 nts labelled with several digoxigenins. The h1.2 hairpin was prepared as previously described in [43]. The stem of the h1.4 hairpin comes from a segment of the plasmid PBR322 and four different oligonucleotides are annealed and ligated to generate the loop and handles (details in Supplementary Fig. S1). Experiments with *E.coli* RecQ were performed with the h1.2 hairpin and experiments with RecG and gp41 were performed with the h1.4 hairpin.

B. Enzyme preparation and experimental conditions

The different helicases, T4 gp41, *E.coli* RecQ and *E.coli* RecG, were purified as previously described [44–46]. In this study, we used a truncated version of the

2

RecQ helicase lacking the HRDC (Helicase and RNase D C-terminal) domain, referred as RecQ-Δ in previous studies [40, 45]. Hereafter, we will simply use the notation RecQ to refer to the RecQ-Δ variant.

Assays with gp41 and RecG were performed in a buffer containing 25 mM Tris–Ac (PH 7.5), 10 mM $Mg(OAc)_2$, 150 mM KOAc, 1 mM dithiothreitol (DTT), and different ATP concentrations (0.5-4 mM for gp41 and 100 μM-2 mM for RecG). Assays with RecQ were performed in a buffer containing 20 mM Tris–HCl (pH 7.5), 25 mM NaCl, 3 mM $Mg(Cl)_2$, 1 mM DTT and different ATP concentrations (40 μM to 1 mM). All experiments were done at 25°C. The protein concentration was 50 nM for gp41 (monomeric concentration), 10 nM for RecG and 30 pM for RecQ. These concentrations were chosen to optimize single-molecule conditions. To do so, we check that the mean duration of a single unwinding trace (typically from a few seconds to a few tens of seconds, depending on the helicase, the ATP concentration and the force conditions) is much smaller than the time between events, typically by a factor $\sim$10. This condition minimizes the probability of events where multiple helicases translocate simultaneously on the same hairpin.

C.   Single-molecule experiments

In magnetic tweezers (MT) experiments, we use a PicoTwist MT instrument (www.picotwist.com) to manipulate DNA hairpins tethered between a micrometric magnetic bead and the glass surface of a microfluidic chamber (Fig. 1 (a)). For making the tethers the glass surface is treated with an anti-digoxigenin antibody and passivated with bovine serum albumin and the micron-sized magnetic beads are coated with streptavidin (Invitrogen MyOne). The applied force is controlled by adjusting the distance between the magnets and the sample (Z_{mag}). The microfluidic chamber is illuminated by a red LED that generates a parallel and monochromatic illumination. Using an inverted microscope connected to a CMOS camera we image the beads. The images are decorated by a set of diffraction rings, enabling real-time tracking of beads' 3D position with nanometric resolution at 30-80 Hz [47, 48]. From the bead's z position we obtain the extension of the DNA molecule. The bead's fluctuations in the $x - y$ plane are used to measure the force via the equipartition theorem [47, 48]. An average calibration curve $F(Z_{mag})$ is used to estimate the force with 10% error due to bead inhomogeneities [48]. In OT experiments, the DNA molecule is tethered between two micron-sized polystyrene beads using biotin-streptavidin and digoxigenin-antidigoxinein bonds. One bead is immobilized on the tip of a micropipette and the second bead is captured in an optical trap generated by two counter-propagating lasers (Supplementary Fig. S4 (a)). The force acting on the bead can be measured from the change in light momentum deflected by the bead using position-sensitive detectors [49]. After injecting the he-

licases and ATP, unwinding and rewinding activities are detected as an increase and decrease of the measured DNA hairpin extension respectively (Fig. 1 and Supplementary Fig. S4).

MT are used to test the activity of helicases in a force range going from 5 to 15 pN. Typically about 50-100 beads are tracked simultaneously which allows us to obtain large statistics. For the unwinding helicases (gp41 and RecQ), we started with the hairpin formed at a force below the unzipping force (15 pN) and monitored the unwinding activity from the DNA extension changes (Fig. 1 b,c). The gp41 helicase requires a long 5' tail for efficient loading [44, 50]. For this reason, we used a 40-mer oligonucleotide that is complementary to a hairpin region located at $\sim$500 bp from the fork. By unzipping the hairpin (at $F > 15$ pN) we hybridized the oligonucleotide, generating a $\sim$500 nt 5' and 3' tails (Supplementary Fig. S2).

For the RecG rewinding helicase, we started with a partially unzipped hairpin. The partially unzipped configuration was achieved by either hybridizing a short oligonucleotide complementary to a hairpin region or by using forces close to the unzipping force. In the former case the force was first increased to mechanically unzip the hairpin and allow the oligonucleotide to bind. Next, the force was decreased to a given value (typically between 5 and 13 pN) and the hairpin partially reforms until reaching the oligonucleotide that blocks the full rezipping (Supplementary Fig. S3 (a)). In the latter case, the force was set to a value ($\sim$ 15 pN) where the hairpin unzips except the last $\sim$50 bases containing a GC-rich region that require larger forces to unzip (Supplementary Fig. S3 (b)). In both cases, the rewinding of the partially unzipped hairpin was detected as a decrease in the measured DNA extension (Fig. 1 and Results).

OT were also used to test the activity of the RecG helicase at larger forces (above 15 pN). In OT assays, we initially increased the distance between the micropipette and the trap (X_T) reaching a force of $\sim$15 pN and a partially unzipped hairpin. In the presence of RecG, the rewinding reaction causes a shortening of the DNA that induces the displacement of the bead in the trap, generating an increase in force (Supplementary Fig. S4 (b)). By using a force feedback protocol we can test the rewinding activity at different forces. We did not observe any activity above $\sim$35 pN, in agreement with previous measurements [38]. These large forces probably induce the stalling and dissociation of the enzyme from the DNA template.

D.   CTRW Model

The movement of the helicase along DNA can be modelled as a one-dimensional random walk on a chain, where the walker can perform different transitions (Fig.2 (a)): forward movement with probability P_+ and step d_+, backward movement with probability P_- and step

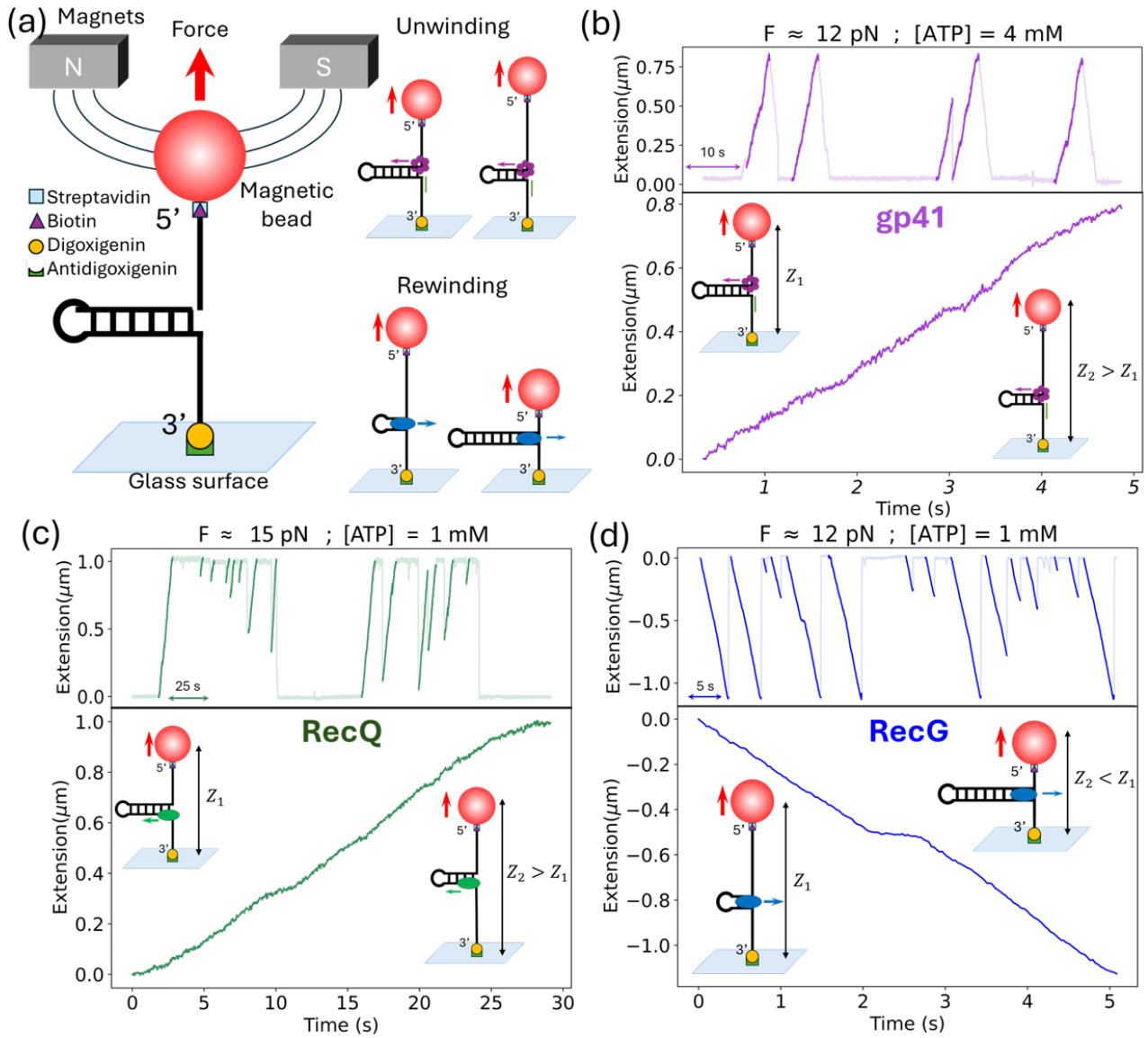3

FIG. 1. **Helicase experiments (a)** Schematic representation of the MT experimental setup, where a DNA hairpin is tethered between a glass surface and a magnetic bead. The progress of the unwinding and rewinding reactions leads to changes in the molecule extension. **(b,c,d)** Top panel: Experimental traces showing the hairpin extension as a function of time for gp41 (purple), RecQ (green) and RecG (blue) helicases. The un(re)winding events are highlighted in dark colour. Bottom panel: Details of a single un(re)winding trace with the schematic representations of the hairpin state at the beginning (left) and at the middle (right) of the trace.

d_- and pausing with probability P_0 and step $d = 0$. These probabilities satisfy the normalization condition: $P_+ + P_- + P_0 = 1$. Each transition is governed by an exponentially distributed intrinsic time with an average value: τ_+ for the forward transition, τ_- for the backward transition, and τ_0 for the pause. This kinetic scheme can be described within the continuous-time random walk (CTRW) framework [51, 52]. In this formalism, the walker dynamics is described using two stochastic distributions: the jump distribution $f(x)$, which represents the probability of a displacement x during a single step and depends on the probabilities P_+, P_- and P_0, and the

waiting time distribution $\psi(t)$, which describes the time interval t before a transition occurs and depends on the intrinsic times τ_+, τ_- and τ_0. The probability of locating the walker at a distance x at a time t, $P(x,t)$, is given by the Montroll-Weiss expression in Fourier-Laplace space (s is the Laplace transform of t and k the Fourier transform of x)[51, 53],

$$P(k,s) = \frac{1 - \hat{\psi}(s)}{s} \frac{1}{1 - \hat{\phi}(k,s)}, \qquad (1)$$

4

where $\hat{\psi}(s)$ is the Laplace transform of the waiting time distribution $\psi(t) = \sum_{i=+,-,0} \frac{1}{\tau_i} e^{-t/\tau_i}$ and $\hat{\phi}(k,s)$ is the Fourier-Laplace transform of the one-step joint distribution $\phi(x,t)$. Taking into account that the waiting time and jumps are correlated: $\phi(x,t) = \psi(t)f(x|t)$, being $f(x|t)$ the conditional probability density function to have a displacement x in a time interval t during a single step. The one-step joint distribution reads as:

$$\phi(x,t) = \frac{P_-}{\tau_-} e^{-t/\tau_-} \delta(x + d_-)$$
$$+ \frac{P_0}{\tau_0} e^{-t/\tau_0} \delta(x)$$
$$+ \frac{P_+}{\tau_+} e^{-t/\tau_+} \delta(x - d_+). \qquad (2)$$

Equation (1) can be analytically solved in the long-time regime ($k \to 0$, $s \to 0$) giving (Supplementary Section V):

$$P(k,s) = \frac{1}{s[1 - ik\frac{a_1}{sE} - ik\frac{a_2 E - a_1 F}{E^2} + \frac{k^2}{2}\frac{c_1}{sE}]}, \qquad (3)$$

with $a_1 = P_+ d_+ - P_- d_-$,
$a_2 = P_+ d_+ \tau_+ - P_- d_- \tau_-$,
$c_1 = P_+ d_+^2 + P_- d_-^2$,
$E = P_- \tau_- + P_0 \tau_0 + P_+ \tau_+$,
$F = P_- \tau_-^2 + P_0 \tau_0^2 + P_+ \tau_+^2$.

Performing the inverse Laplace-Fourier transform we obtain a Gaussian distribution of displacements and times with an average velocity v and a diffusivity D given by:

$$v = \frac{a_1}{E}, \quad D = \frac{c_1}{2E} + \frac{a_1}{2E^2}(a_2 E - a_1 F). \qquad (4)$$

Details of the model are presented in Supplementary Section V.

E.   Data analysis

The DNA extension as a function of time measured in MT (Fig.1 (b, c, d) upper panels) and OT experiments (Supplementary Fig. S4 (b)) has been converted from nm to bp by using a conversion factor that depends on the force applied. This factor is obtained from the elastic properties of the ssDNA molecule [54] as described in Supplementary Figure S5. In MT experiments, multiple tethers could be tracked simultaneously in a single experiment (~50), each tether typically exhibiting $\sim$ 10-50 unwinding/rewinding traces. In OT different tethers were tested successively. Typically we used about 3-5

tethers, each presenting $\sim$ 5-20 traces. For each tether (in MT or OT) we computed the average velocity v and the diffusivity D. The velocity was determined as the slope of the linear fit of the mean displacement over time, $\langle \Delta x \rangle = vt$ (top insets Fig. 3 (a,c, e)). The diffusivity was determined as half of the slope of the linear fit of the mean square displacement (MSD) over time, $\langle \Delta x^2 \rangle = 2Dt$ (bottom insets Fig. 3 (a,c and e)). The MSD presented an initial regime (at very low times) that deviates from the linear behaviour due to the Brownian motion of the bead (Supplementary Fig. S6) [33]. We then performed the fits with a time offset of few milliseconds.

We also analysed the pauses along the experimental traces by using a pause detection algorithm based on change point detection [55] (Fig. 3 (b,d,f) and Supplementary Section VI). The algorithm depends on several parameters that are chosen based on the intrinsic noise level of the experimental traces (Supplementary Section VI). Nevertheless, sensitivity to short or long pauses depends strongly on the chosen parameters: optimizing for short pauses can fragment long ones, while detecting long pauses can lead to missing short events. To address this challenge, we optimized the parameters to reliably detect long pauses and analysed only those pauses longer than a threshold time τ_s. Assuming that pause durations follow an exponential distribution, we fitted the histogram of detected pauses above τ_s to extract the characteristic pause time. The threshold τ_s was determined as the point where the histogram begins to deviate from exponential behaviour and typically corresponds to a short time on the order of the second or a fraction of a second. This method is illustrated in Supplementary Figure S9. To further validate this procedure, we simulated the continuous-time random walk (CTRW) model with the parameters shown in table III and using the pause detection and histogram fitting protocol, we successfully recovered the theoretical predictions of our model (Equation 7) within a $\sim$ 5% accuracy (Supplementary Section VI and Fig. S11). We further checked the robustness of the pause detection analysis by tuning the algorithm parameters (Supplementary Section VI) and using an alternative velocity analysis (Figs. S12 S13 and S14). The experimental histogram of pausing times fitted to an exponential distribution is used to obtain the characteristic time to exit the pause, $\langle t_{-p} \rangle = \frac{1}{k_{-p}}$ (top insets Fig. 3 (b,d and f)). The time lag between pauses also follows an exponential distribution (bottom insets Fig. 3 b,d and f), yielding a value for the characteristic time to enter the pause $\langle t_p \rangle = \frac{1}{k_p}$. For each helicase, the velocity v, diffusivity D and pause kinetics, k_{-p} and k_p, at each experimental condition ([ATP] and force) were computed as the average value between different tethers, typically ~10-50 tethers.
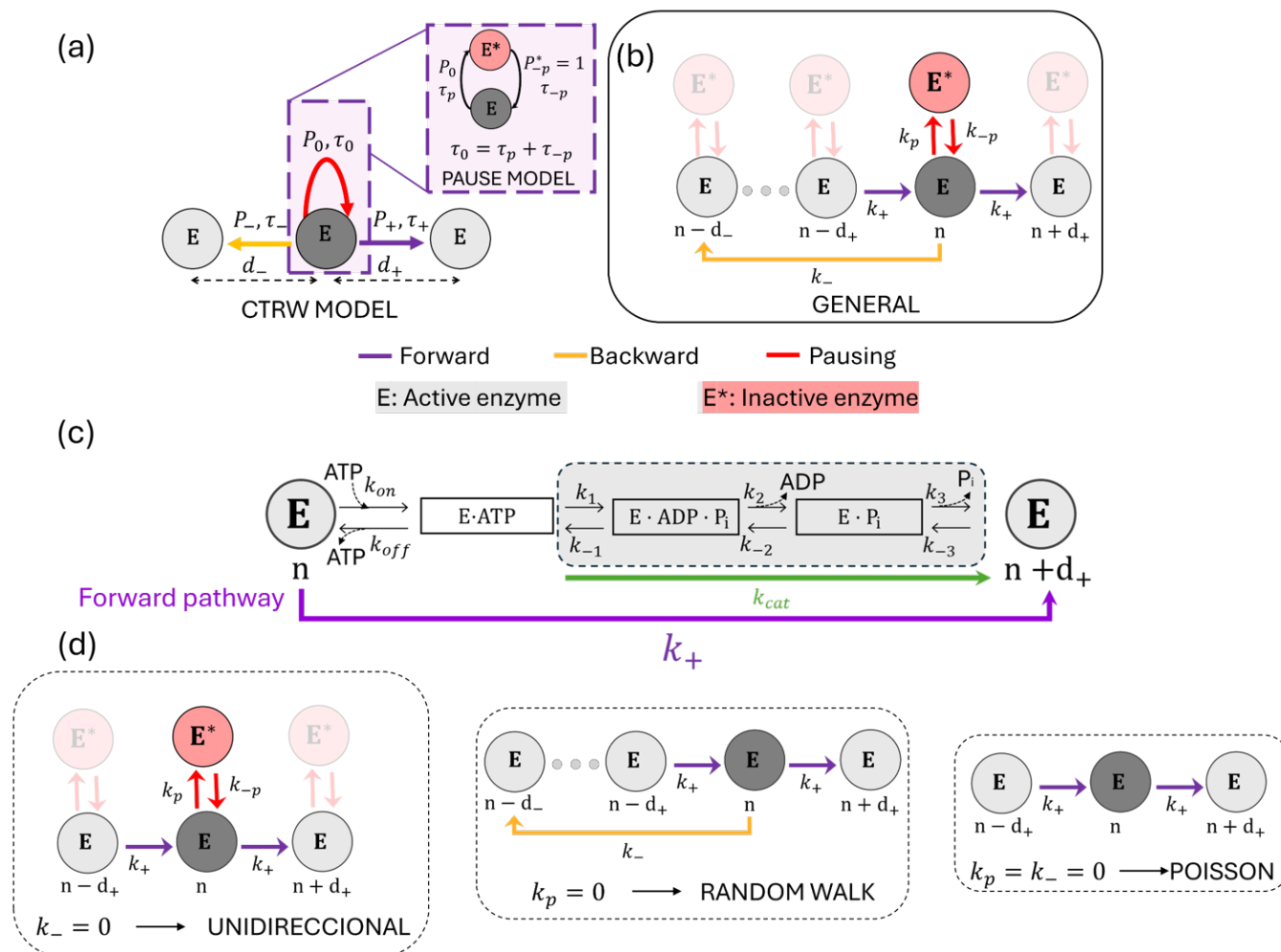
5

FIG. 2. **Helicase models.** **(a)** Diagram of the CTRW model used to describe helicase motion. Inset shows the diagram of the pause transition divided into two steps corresponding to entering and exiting the pause state. E and E^* represent the states of a translocation-active and a pause-inactive helicase **(b)** Diagram of the general model with kinetic rates, which includes three pathways: the forward ATP-hydrolysis coupled to translocation on-pathway transition (purple), the off-pathway backward transition (yellow) and the off-pathway pausing transition (red). Kinetic rates and distances between states are indicated for each transition. **(c)** Details of the forward ATP-hydrolysis coupled to the translocation pathway indicating the intermediate steps. The overall rate k_+ (purple) integrates the ATP binding and unbinding reaction as well as the ATP hydrolysis and release of ADP and Pi. The ATP hydrolysis reaction (grey shaded area) is highly irreversible and can be approximated with a single kinetic rate k_{cat} (green). **(d)** Sub-models derived from the general model: the unidirectional model (without backward motion, $k_- = 0$), the random walk (absence of off-pathway pausing state, $k_p = 0$) and the Poisson model ($k_- = 0$ and $k_p = 0$).

III.   RESULTS

To investigate the activity of helicases, we used magnetic and optical traps to mechanically manipulate a DNA hairpin while monitoring the changes in DNA extension as the helicase unwinds or rewinds the hairpin. In MT experiments, the DNA hairpin was tethered between a glass surface and a micron-sized magnetic bead, and force was applied using a couple of magnets located on top of the microfluidic chamber (Fig. 1 (a)). In OT

experiments, the DNA hairpin was tethered between two micron-sized beads, one held in an optical trap and the other fixed on the tip of a micro-pipette (Supplementary Fig. S4). In both assays, a mechanical force was applied to destabilize the DNA hairpin duplex serving as a means to either assist the advance of a DNA unwinding helicase or hinder the rewinding activity of a DNA rewinding helicase. Details of the single-molecule experiments are presented in Section II C in Methods.
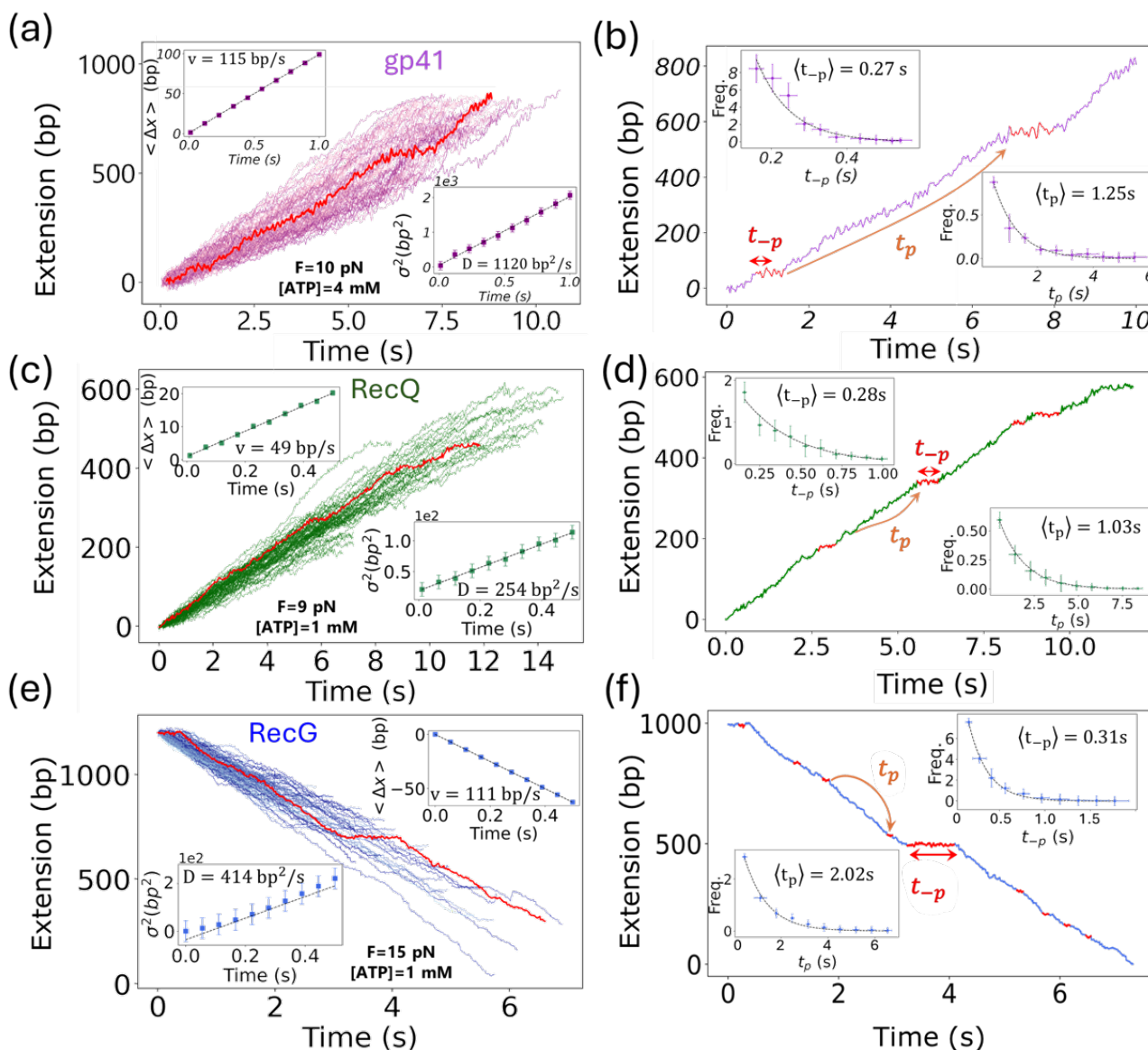
6

FIG. 3. **Helicase velocity, diffusivity and pause kinetics. (a,c,e)** Set of experimental traces (~ 50) showing the DNA extension in bps as a function of time for gp41 (purple), RecQ (green) and RecG (blue). A single trace is shown in red as an example. Insets show the mean and variance of the helicase displacement as a function of time, computed from all traces in the main plot. Linear fits are shown as straight lines. Error bars are the standard error of the mean. **(b,d,f)** A single experimental trace for gp41 (purple), RecQ (green) and RecG (blue), showing the pauses detected with the step-finding algorithm in red. Insets show the distribution of the pause time t_{-p} (top) and the time between pauses t_p (bottom) from all the traces in panels (a), (c) and (e). Exponential fits are shown as a continuous lines. Error bars are estimated using the bootstrap method.

A.   Measuring DNA unwinding and rewinding activities

A force above $\sim$15 pN mechanically unzips the hairpin (Supplementary Fig. S2). Below $\sim$15 pN, where the hairpin is mechanically stable, we can monitor the DNA unwinding catalysed by helicases that was detected as a smooth increase in the measured extension (Fig. 1 (b) and (c)). Unwinding activity was measured using MT to track different DNA hairpins in parallel, increasing the statistics. Here, we studied two different unwinding helicases: gp41 and RecQ. The gp41 is a hexameric helicase from the T4 bacteriophage that promotes DNA unwinding during DNA replication [39, 44], whereas the RecQ is a monomeric helicase from *E.coli*, playing a central role in DNA repair [40, 41]. For studying DNA rewinding helicases, we combined MT and OT experiments, as done in previous works [38], to explore different force regimes (MT from 5 to 15 pN and OT above 15 pN).

7

In these experiments, we first pulled the extremities of the tethered DNA molecule to partially unzip the hairpin ($\sim$ 15 pN). The enzyme's rewinding (or annealing) activity was detected as a decrease in the DNA extension both in MT and OT assays (Fig. 1 (d) and Supplementary Fig. S3 and Fig. S4). Here, we studied RecG, which is a monomeric helicase from *E.coli* that promotes the rewinding of DNA strands into duplex DNA [38, 42]. When the rewinding activity is coupled to DNA unwinding, it leads to the formation of a Holliday junction a four-way DNA structure that is the central intermediate in different DNA repair and recombination pathways [56].

The measured changes in DNA extension can be converted into a number of unwound/rewound bps from the elastic response of the ssDNA (Supplementary Fig. S5). This allows to infer the position of the helicase along the DNA (in bp units) as a function of time, as shown in Figure 3. From these traces, we measured the mean and variance of the helicase displacement and extract the helicase velocity and diffusivity (insets in Fig. 3 (a,c,e) and Methods section II E).

B.   Measuring helicase ssDNA translocation activity

Interestingly, in some cases, we can also monitor the motion of the helicase while it translocates along one strand of ssDNA. In gp41 assays, the experimental traces showed a triangular shape (Fig.1 (b) upper panel and Supplementary Fig. S2), where the rising edge corresponds to the helicase unwinding the hairpin, as previously discussed. After the enzyme reaches the loop and the hairpin has been fully unzipped, the helicase can continue translocating on ssDNA while the hairpin reanneals in its wake. In this latter process, the DNA hairpin rewinding reaction, observed as a decrease in the measured DNA extension, is limited by the enzyme translocation. We can then infer the position of the helicase as a function of time in the ssDNA translocation process and estimate the helicase velocity and diffusivity, as done with the unwinding traces. For RecQ, the falling edge was not observed (Fig.1 (c) upper panel) because RecQ displays strand switching and repeated unwinding when reaching the loop [40, 57]. This directed motion towards unwinding precluded the detection of the RecQ ssDNA translocation motion. For RecG, we measured its ssDNA translocation activity by performing experiments at low forces using short oligonucleotides to transiently block the DNA fork (Supplementary Fig. S3 (a) and [38]). After the bound oligonucleotide was displaced, the hairpin's rewinding proceeds at a constant velocity, as given by the translocation motion of the helicase. These low-force traces allowed to measure the RecG velocity and diffusivity on ssDNA.

C.   Model for helicase movement

The motion of helicase along DNA driven by the nucleotide hydrolysis reaction can be described as a random walk on a one-dimensional chain. Translocation is governed by a set of kinetic reactions that connect different helicase-nucleotide states (or conformations) along the DNA chain. The simplest scenario is given by a Poisson model, in which the helicase moves along the DNA in discrete steps of size d_+ with exponentially distributed waiting times. The average velocity of the enzyme is given by $v = d_+/\tau = d_+ k_+$, where τ and its inverse k_+ are the characteristic waiting time and the forward kinetic rate respectively. The Poisson description is, in general, too simple to capture the dynamics observed in helicases. This is because most helicases exhibit complex mechano-chemical cycles with different rate-limiting steps and multiple pathways. In particular, studies with different helicases have shown the presence of pauses along the helicase trajectories generated by off-pathway states [24, 25, 27, 58]. Besides pauses, there are backward steps. In some cases, these backward steps represent intermediate transitions within forward steps [26, 28]; in other cases, backward steps reflect slippage events, where the enzyme loses contact with the DNA strand and moves back several bases [13, 27, 59–61].

Here we propose a minimal CTRW model that incorporates the key features of helicase movement, including forward and backward steps and pauses. In the CTRW model (Fig.2 (a)), transitions are chosen with a probability P_+ to move right, P_- to move left, and P_0 to enter the pause state with exponentially distributed times of average τ_+, τ_- and τ_0, respectively. For simplicity we assume that forward and backward transitions are characterized by constant steps, d_+ and d_- respectively. Using the CTRW framework we can compute the average velocity and diffusivity as a function of the probabilities $P_{+,-,0}$, the transition times $\tau_{+,-,0}$ and the step-sizes $d_{+,-}$, (Eqs.3,4) (Supplementary Section V and Methods Section II D). In the context of chemical reactions, kinetic rates k_i are used instead of probabilities P_i and intrinsic transition times τ_i. To express the model in terms of kinetic rates, we consider the following assumptions (Fig.2 (a)): (i) The on-pathway forward reaction and the off-pathway backward (slippage) reaction are irreversible, with rates given by $k_+ = P_+/\tau_+$ and $k_- = P_-/\tau_-$, respectively; (ii) The off-pathway pause transition is characterized by pause entry and exit rates, given by $k_p = P_0/\tau_p$ and $k_{-p} = 1/\tau_{-p}$, with $\tau_0 = \tau_p + \tau_{-p}$; (iii) The intrinsic transition time from the initial state to any other state is assumed to be the same for all transitions $\tau_+ = \tau_- = \tau_p = \tau \ll \tau_{-p} \rightarrow \tau_0 \sim \tau_{-p}$ (Supplementary Section V for details).

The kinetic scheme is shown in Fig. 2 (b) and includes three transitions: the ATP-driven forward transition (purple arrow), the slippage backward transition (yellow arrow), and the pausing transition (red arrows). The two first transitions are irreversible and connect dif-

8

ferent positions of the active helicase state (E) along the DNA track. The third one connects the active helicase state (E) with the pause-inactive one (E*). The ATP-hydrolisis forward transition includes several intermediates as depicted in Fig. 2 (b), but it is described with a single rate, k_+, that includes ATP binding-unbinding and ATP hydrolisis. Using the CTRW formalism we can write the average velocity and diffusivity as a function of the kinetic rates as (Section II D in Methods):

$$v = \frac{a_1}{E} \qquad (5)$$

$$D = \frac{1}{2E}\left[c_1 + 2\left(\frac{a_1}{E}\right)^2 \frac{k_p}{k_{-p}}\left(\frac{1}{k_p} - \frac{1}{k_t}\right)\right] \qquad (6)$$

$$k_t = k_+ + k_- + k_p$$
$$E = \frac{k_+}{k_t} + \frac{k_-}{k_t} + \frac{k_p}{k_{-p}}$$
$$a_1 = k_+ d_+ - k_- d_-$$
$$c_1 = k_+ d_+^2 + k_- d_-^2$$

In general, the different kinetic rates can depend on the concentration of the various reactants (enzyme (E), ATP, ADP, inorganic phosphate P_i) and the applied force on the experiment. As discussed in Supplementary Section VIII, a general expression for the rates k_i is given by:

$$k_i = \frac{k_{cat}^i[ATP]}{K_M^i + [ATP]} e^{\frac{x_i^\dagger(F - F_c)}{k_B T}}, \quad \text{un(re)winding}$$
$$k_i = \frac{k_{cat}^i[ATP]}{K_M^i + [ATP]}, \quad \text{translocation} \qquad (7)$$

with $i = +, -, p, -p$. Based on a Bell-like model description [62], the rates are exponential with the force F times a transition state distance $x_i^\dagger$, which is related to the change in DNA extension along the kinetic step i. The expression (7) assumes that the force only affects the helicase unwinding/rewinding activity, but not the helicase translocation along ssDNA, where we take $x_i^\dagger = 0$. At $F_c \sim 15$pN, where the hairpin mechanically unzips, the helicase velocity reduces to the translocation velocity that only depends on [ATP]. The ATP dependence is based on a Michaelis-Menten expression [63] where k_{cat}^i is the rate at ATP saturating conditions and K_M^i is the Michaelis-Menten constant defined as the ATP concentration where the reaction velocity is $k_{cat}/2$. Note that depending on the values of K_M^i and k_{cat}^i, the transitions associated with a specific rate k_i would (i) involve ATP hydrolysis (finite K_M^i and k_{cat}^i), (ii) involve ATP binding but not hydrolysis ($K_M^i \gg [ATP]$), or (iii) not depend on the ATP ($K_M^i \ll [ATP]$). These different scenarios are explored during the model fitting process (see next section).

D.   Best-fitting model

The general model proposed (Fig.2 (b)) considers forward and backward steps of size d_+ and d_- and four different kinetic rates, k_+, k_-, k_p, and k_{-p}. The rates have their [ATP] and force dependence, as described by Eq.7, through three independent parameters: K_M, k_{cat}, and $x^\dagger$ summing up to 14 different free parameters. The model includes several simplified cases: the Unidirectional model (Uni-model) without backtracking ($k_- = 0$), the Random walk model (RW-model) without pausing ($k_p = 0$), and the Poisson model described above ($k_- = k_p = 0$), involving 10, 8, and 4 free parameters, respectively. They are schematically shown in Figure 2 (d).

To reduce the number of free parameters we have analysed the helicase pauses separately. Using a pause detection algorithm [55] (Supplementary Section VI and Fig. S10), we measure the waiting times to enter and exit pauses, t_p and t_{-p}. Both times follow an exponential distribution (insets in Fig. 3 (b,d,f)), from which we derive the average time to enter and to exit the pause, $\langle t_p \rangle$ and $\langle t_{-p} \rangle$, and the corresponding rates $k_p = 1/\langle t_p \rangle$ and $k_{-p} = 1/\langle t_{-p} \rangle$ (Section II E in Methods). The exponential behaviour agrees with the single-rate limiting step assumption for a single pause state. Lower panels of Figure 4 (a, c, e) show k_p and k_{-p} as a function of the applied force for the three enzymes. Rates are exponentially dependent on force as predicted by Eq. 7. The ATP dependence is also well described using the same equation. The overall fit of the force and ATP dependent rates k_p and k_{-p} to Eq. 7 allows determining the values of k_{cat}^p, K_M^p, $x_p^\dagger$, k_{cat}^{-p}, K_M^{-p} and $x_{-p}^\dagger$, reducing the number of model parameters from 14 to 8 for the general model and from 10 to 4 for the Uni-model. The number of fitting parameters for the RW-model and the Poisson model remains unchanged as they do not consider pauses.

To select the best model that fits the experimental velocity and diffusivity data with the least number of parameters, we performed a least-squares minimization of the reduced chi-square (χ_ν^2) value minus 1, where ν stands for the number of degrees of freedom of the fit, equal to the number of data points minus the number of fitting parameters. The goal is to obtain a value of χ_ν^2 as close as possible to 1. Values of $\chi_\nu^2 \gg 1$ indicate a poor model fit, and $\chi_\nu^2 \ll 1$ indicate over-fitting. We also used the Akaike Information Criterion (AIC) and the Bayesian Information Criterion (BIC) [64, 65], that are statistical tools for model selection; they give a numerical value that balances the goodness of the fit with the number of parameters (Supplementary Section VII).

We fitted the general model and the three sub-models (Uni, RW, and Poisson) to the experimentally measured velocity and diffusivity of the three helicases studied: gp41, RecQ, and RecG (Fig. 4 (a,c,e), upper panels). For each helicase and model, we obtained the AIC and BIC values (Table II), selecting the best-fitting model as the model with lowest AIC/BIC values ensuring $\chi_\nu^2 \approx 1$.

For the three helicases, the fits to the RW and Poisson models lead to $\chi_\nu^2 >> 1$, showing that these models fail to reproduce the experimental data (Table II and Supplementary Fig. S15). In other words, in the absence of an off-pathway pause state, we cannot reproduce simultaneously the measured helicase velocity and diffusivity.

The best-fitting model for RecQ is the general model. For gp41 and RecG both the Uni-model and the general model fit the data with similar values of χ_ν^2, AIC and BIC (less than 10% differences in their values, Table II). Note that the difference between the two models is that the general model includes a backward slippage pathway, whereas the Uni-model does not. Helicase slippage has been previously observed for gp41 [13, 59], RecQ [27] and other helicases [60, 61]. Moreover, large slippage events (> than 10bp) are observed in our experimental traces for the three helicases (Supplementary Fig. S18), but they are not included in the velocity and diffusivity analysis. However, smaller slippage events might be masked in the experimental signal. As a consequence we choose the general model for the three helicases.

Once the model had been selected, we performed a second optimization step for each helicase type by identifying weak dependencies on force and [ATP] of the rates k_+, k_-, k_p, k_{-p} in Eq. 7. We have tested $x^\dagger = 0$ for the rates that weakly depend on force and $K_M = 0$ for the rates that weakly depend on concentration, further reducing the number of parameters. In Table II and Figure 4 we show, for the three helicases, the results from the overall optimization process that leads to the best model with the minimum number of parameters. For RecQ we only used unwinding data, whereas for gp41 and RecG we simultaneously fitted the average velocity and diffusivity using un(re)winding and ssDNA translocation data. Interestingly, for the ssDNA translocation activity, the measured velocity and diffusivity are independent of force for both helicases (Fig. 4 grey shaded area). This finding supports the view that the main role of the mechanical force is altering the duplex stability, therefore affecting the DNA un(re)winding reaction but not the enzyme translocation along ssDNA.

For all helicases, the forward rate k_+ depends on [ATP], with its Michaelis-Menten constant, K_M^+, very close to the K_M obtained by fitting the average un(re)winding velocity as a function of [ATP] using the Michaelis-Menten expression: $v = \frac{k_{cat}[ATP]}{K_M+[ATP]}$ (Supplementary Fig. S16 and Table III). This shows that the main ATP dependence comes from the on-pathway ATP hydrolysis coupled with the translocating forward step. In contrast, the force dependence is different for each helicase. For RecQ and RecG, k_+ is weakly dependent on force, whereas for the gp41, k_+ markedly increases with force (Table III), in agreement with the reported active and passive character of these helicases, respectively [13, 38]. On the other hand, the pause kinetics have specific ATP and force dependencies for each helicase. In particular, the pause kinetics only depend on the ATP concentration for the RecQ case, in agreement with

previous measurements [27]. An ATP-dependent pause kinetics has been observed in other enzymes [24, 66]. Mechanistically, ATP-dependent transitions into or out of paused states may reflect conformational rearrangements of the helicase that require nucleotide binding or hydrolysis [67–69].

The model can be fitted to the experimental data (velocity and diffusivity) with similar values of $\chi_\nu^2 \approx 1$ using a large range of k_+ and d_+ values, which are almost inversely correlated. To limit the range of step-sizes, we explored different values around each AIC/BIC minimum and identified a spectrum of values compatible with a relative difference of less than 5% in both AIC and BIC. This analysis lead to step-sizes of $d_+ = 1-3$ bp for gp41, $d_+ = 0.5-1$ bp for RecQ, and $d_+ = 3-4$ bp for RecG. Interestingly, these values are in agreement with previously estimated step-sizes for these helicases: $d_+ = 1$ for gp41 or other hexameric helicases [39, 60, 70]; $d_+ = 1$ for RecQ [58, 71] and $d_+ = 2-4$ for RecG [38, 72, 73]. Accordingly, we have chosen $d_+ = 1$ for gp41 and RecQ, and $d_+ = 3$ for RecG. Finally, the backward slippage transition is described with a force and ATP independent rate k_- and a backward step $d_- \sim 2-4$ bps for the three helicases. Recent studies suggest that some helicases might display a variable step-size [74]. On the other hand, helicase slippage occurs along a random number of nt in ATP and force dependent manner ([59] and Supplementary Fig. S18). Therefore the model could be refined by considering variable forward and step-sizes d_+ and d_-, with force and ATP dependencies.

	k_+	k_-	k_p	k_{-p}
gp41	F: **Yes**	F: **No**	F: **Yes**	F: **Yes**
	[ATP]: **Yes**	[ATP]: **No**	[ATP]: **Yes**	[ATP]: **No**
RecQ	F: **No**	F: **No**	F: **Yes**	F: **Yes**
	[ATP]: **Yes**	[ATP]: **No**	[ATP]: **No**	[ATP]: **Yes**
RecG	F: **Yes**	F: **No**	F: **Yes**	F: **Yes**
	[ATP]: **Yes**	[ATP]: **No**	[ATP]: **No**	[ATP]: **No**

TABLE I. Force and ATP dependencies of the rates involved in equation S.17 for the three studied helicases. A schematic diagram is shown in Figure 4 (b,d,f) with the corresponding dependencies.

E.   On the efficiency of helicases

The trade-off between the energy cost and the efficiency of helicases can be investigated through the thermodynamic uncertainty relation (TUR) [35]. The TUR is an inequality relating the uncertainty (or precision) in
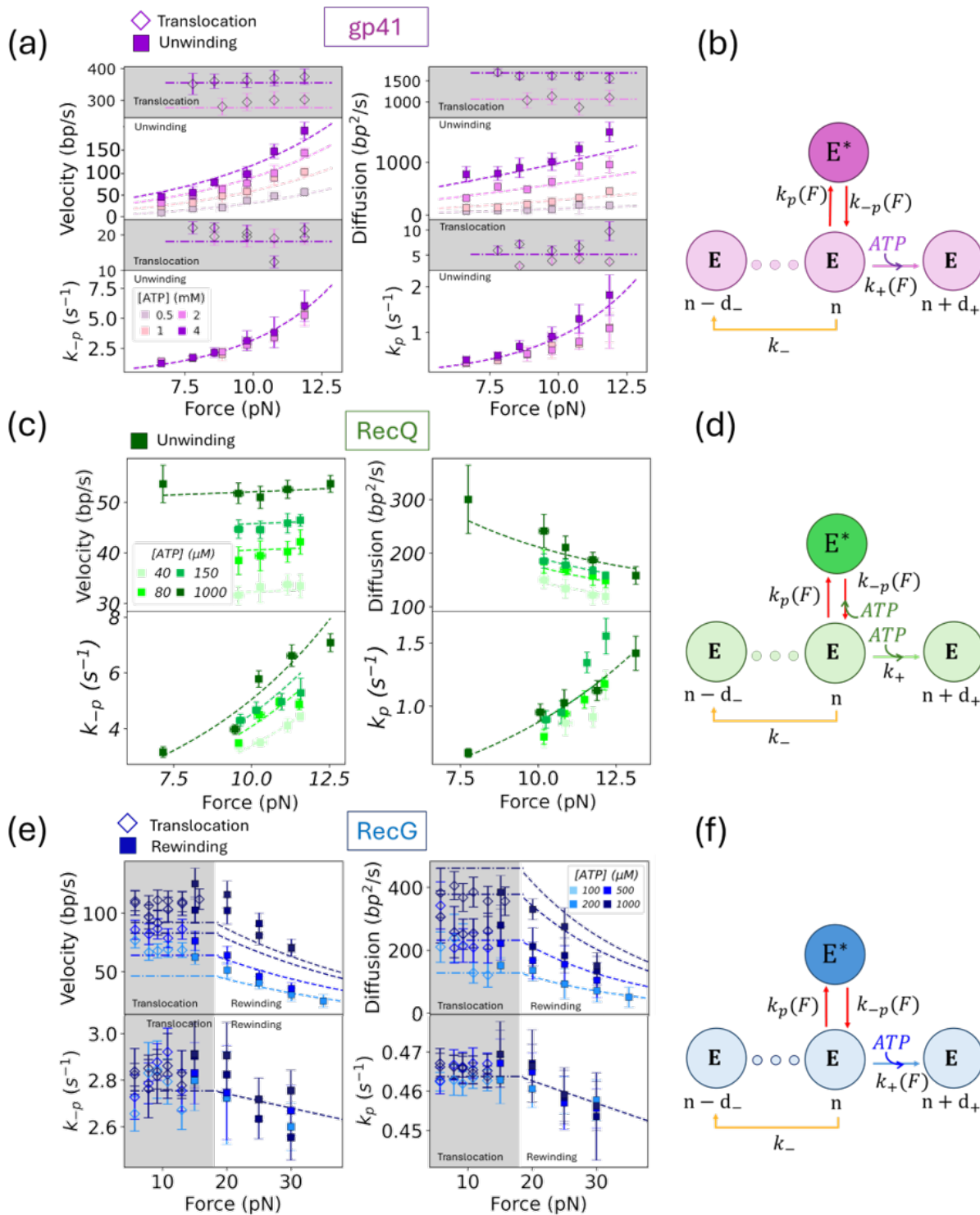
10

FIG. 4. **Best-fitting models (a,c,e)** The measured velocity (top left), diffusivity (top right), exit pause rate (bottom left), and entry pause rate (bottom right) as a function of force at different ATP conditions for gp41 (purple), RecQ (green), and RecG (blue). The filled squares and empty diamonds are computed from the un(re)winding and translocation data respectively. Values shown are the mean between different molecules and the error bars represent the standard error of the mean. For gp41 we average ∼20 beads with ∼20 traces for each bead, for RecQ ∼10 beads with ∼10 traces each and for RecG ∼10 beads with ∼10 traces each. The dashed lines are the best fit to the model, as given by Eqs.(5,6). **(b,d,f)** Schematic refpresentation of the best-fitting model, showing the ATP and force dependence of the different kinetic rates.

Enzyme	gp41			RecQ			RecG		
Estimator	χ^2_ν	AIC	BIC	χ^2_ν	AIC	BIC	χ^2_ν	AIC	BIC
General	**1.77**	**999**	**1013**	**1.32**	**24**	**35**	**2.12**	**1137**	**1158**
Uni	2.01	1053	1062	10	158	165	2.62	1140	1162
RW	8	1309	1331	9	82	94	5	1298	1210
Poisson	16	1493	1502	11	165	173	27	1526	1435

TABLE II. Comparison of models using χ^2_ν, AIC, and BIC. In bold we marked the best values of the estimators.

Parameter	gp41 (d_+ =1 bp)	Error	RecQ (d_+ =1 bp)	Error	RecG (d_+ =3 bp)	Error
k^+_{cat} (s^{-1})	644	5	101	3	33	1
K^+_M (μM)	1700	50	20	3	110	21
x_+ (pm)	190	10	-	-	-30	1
k^-_{cat} (s^{-1})	4.1	0.9	4.9	0.3	1.4	0.1
K^-_M (mM)	-	-	-	-	-	-
x_- (pm)	-	-	-	-	-	-
k^p_{cat} (s^{-1})	5.08	0.01	1.71	0.02	0.46	0.01
K^p_M (mM)	-	-	-	-	-	-
x_p (pm)	305	11	163	5	-2.0	0.2
k^{-p}_{cat} (s^{-1})	18.13	0.04	9.15	0.07	2.75	0.08
K^{-p}_M (mM)	-	-	0.02	0.08	-	-
x_{-p} (pm)	312	3	165	12	-1.9	0.1
d_- (bp)	4	1	4	1	2	1

TABLE III. Parameters obtained from fitting unwinding and translocation data shown in Figure 4 using the best-fitting model protocol described in section III D. Errors extracted from the standard deviation of the parameters obtained performing the fitting several times.

the motor activity and the energy from ATP hydrolysis that is irreversibly lost to the environment as heat q, known as the entropy production rate $\sigma = \dot{q}/T$. For an arbitrary current $\dot{x}$ in a nonequilibrium steady state, the time-integrated current $X(t) = \int_0^t \dot{x}(s)ds = x(t) - x(0)$ satisfies the TUR inequality [75]:

$$\sigma \geq \frac{2\langle X(t)\rangle^2}{V_{X(t)}t}k_B, \tag{8}$$

where $\langle X(t)\rangle$ and $V_{X(t)} = \langle X(t)^2\rangle - \langle X(t)\rangle^2$ are the mean and variance of the integrated current measured during a time interval t. From Eq.(8) one can define the dimensionless $\mathcal{Q}$ factor that quantifies the tightness of the TUR inequality [35],

$$\mathcal{Q} = \frac{\sigma V_{X(t)}}{k_B \langle X(t)\rangle^2}t \geq 2. \tag{9}$$

For helicases, X is the motor displacement measured by the bead's position. From the velocity $v = \frac{\langle X(t)\rangle}{t}$ and diffusivity $D = \frac{V_{X(t)}}{2t}$ we get,

$$\mathcal{Q} = \sigma \frac{2D}{k_B v^2} \geq 2. \tag{10}$$

Previous studies have shown that, for translocating motors, the TUR bound is loose with $\mathcal{Q}$ values ranging from 5 to 20 for kinesin, from 5 to 13 for myosin, or from 50 to 100 for T7 DNA polymerase and the ribosome

[35, 76–78]. However, to our knowledge, $\mathcal{Q}$ has never been investigated for helicases. To determine $\mathcal{Q}$, we measure v and D from the time traces of the motor. In addition, σ can be estimated assuming a tight mechano-chemical coupling between the unwinding-rewinding of d_+ bps and the hydrolysis of one ATP [61, 79]. Moreover, we assume that ATP is not consumed in the backward and pausing steps. If q is the heat per step irreversibly lost to the environment, σ can be written as: $\sigma = \frac{q}{T}\frac{v}{d_+}$ with $d_+ = 1$bp for gp41 and RecQ and $d_+ = 3$bp for RecG. Besides the heat q, the energy balance contains the chemical ($\Delta\mu$) and mechanical contributions (W), $q = \Delta\mu - W$, where $W = d_+(\Delta G_{bp} + W_F)$ is the reversible mechanical work needed to unzip or rezip d_+ bp at force F (Supplementary Fig. S17 and Section IX). ΔG_{bp} is the hybridization or melting free energy per bp, $\Delta G_{bp} \approx 2k_BT$ [80], and W_F is the stretching contribution at force F, which can be estimated using elastic models for the ssDNA polymer (Supplementary Section IX). Finally, the energy released from ATP hydrolysis $\Delta\mu \approx 12 - 20k_BT$, depending on the ATP concentration.

The $\mathcal{Q}$ factor is related to the thermodynamic efficiency. The second law implies $\sigma \geq 0$, and therefore $q \geq 0$ or $W \leq \Delta\mu$. We define the motor efficiency η as the ratio between the amount of mechanical work per step W and the available chemical energy from ATP hydrolysis $\Delta\mu$, $\eta = \frac{W}{\Delta\mu}$. Using the energy balance, $q = \Delta\mu - W$ we can

12

write the efficiency as,

$$\eta = \frac{W}{\Delta\mu} = \frac{1}{1 + q/W} = \frac{1}{1 + \frac{\sigma T d_+}{vW}}, \qquad (11)$$

For the case of a molecular motor un(re)winding DNA, $\mathcal{Q}$ is proportional to σ (Eq. (10)) and η can be written as [35, 36]:

$$\eta = \frac{1}{1 + \mathcal{Q}\frac{vd_+}{2D}\frac{k_B T}{W}}. \qquad (12)$$

To calculate $\mathcal{Q}$ and η we use Eqs.(10,11) using the measured values of v, D and the estimated σ. In Figure 5 we show $\mathcal{Q}$ and η for the three studied helicases in a log-log scale, as a function of the ATP concentration at different forces. RecQ and gp41 present large $\mathcal{Q}$ values $100 - 200$ and $200 - 500$, respectively, and low efficiencies at zero force around 0.1, which further decrease with force. In contrast, RecG has lower $\mathcal{Q}$ values $\sim 10 - 20$, which decrease upon increasing the force above F_c. Interestingly, lower $\mathcal{Q}$ values correlate with higher η, with RecG reaching an efficiency close to 1 at the stalling force of $\sim 35 - 40$pN [38]. In the inset of Fig 5 (b), we plot η versus $\mathcal{Q}$ in a linear-log scale. While gp41 and RecQ fall at the bottom right inefficiency corner of high $\mathcal{Q}$ -low η values, RecG follows a trend with η increasing upon decreasing $\mathcal{Q}$, approaching its maximum $\eta = 1$ if $\mathcal{Q} \to 2$. A two-parameter fit to the function $\eta = 1 + a\log(\mathcal{Q}/2) + b\log^2(\mathcal{Q}/2)$ gives $a = 0.12$, $b = -0.17$ (inset, continuous black line). The significance of this fit lies in the logarithmic dependence of η with $\mathcal{Q}$, underlying a fundamental looseness of the TUR regarding the thermodynamic efficiency of molecular machines. Comparing the unwinding helicases, RecQ, and gp41, we observe that $\mathcal{Q}$ depends on the passive and active nature of the enzymes with larger $\mathcal{Q}$ values for passive helicases, yet η remains qualitatively similar. This is due to the fact that the helicase mechanism (passive versus active) affects the values of D and v (Supplementary Fig. S7 (a)), and consequently the value of the $\mathcal{Q}$ factor. However, the balance between the energy available from ATP hydrolysis and the work, which governs η, does not explicitly depend on D and v: $\eta = \frac{W}{\Delta\mu} = \frac{d_+(\Delta G_{bp} + W_F)}{\Delta\mu}$. Indeed, at a given force F and ATP concentration, η is mainly governed by the helicase step-size, with larger step-sizes leading to higher η values.

From the velocity and diffusivity measurements we can also estimate the random parameter [32], which, in simple cases, is related to the number of rate-limiting steps in an enzymatic cycle. It is defined as $r = \frac{2D}{dv} = \frac{\mathcal{Q}k_B T}{q}$. The results for r are shown in the inset of Fig. 5 (a) for the different enzymes and different experimental conditions. It is interesting to note that, in general, r is larger than one, which is associated with increased motor diffusivity. Both DNA sequence heterogeneity and the presence of pauses can lead to large D values [81]. In order to investigate how the interplay between DNA sequence

and pauses affect the helicase diffusivity we have performed simulations of CTRW model including the DNA sequence of the hairpin substrate. The results show that, for the helicases studied, the effect of pauses largely predominates over the DNA sequence effects. As shown in the Supplementary Section IV, the diffusivity D increases strongly in the presence of pauses, whereas the DNA sequence does not significantly affect its value (Supplementary Fig. S7 (b)).
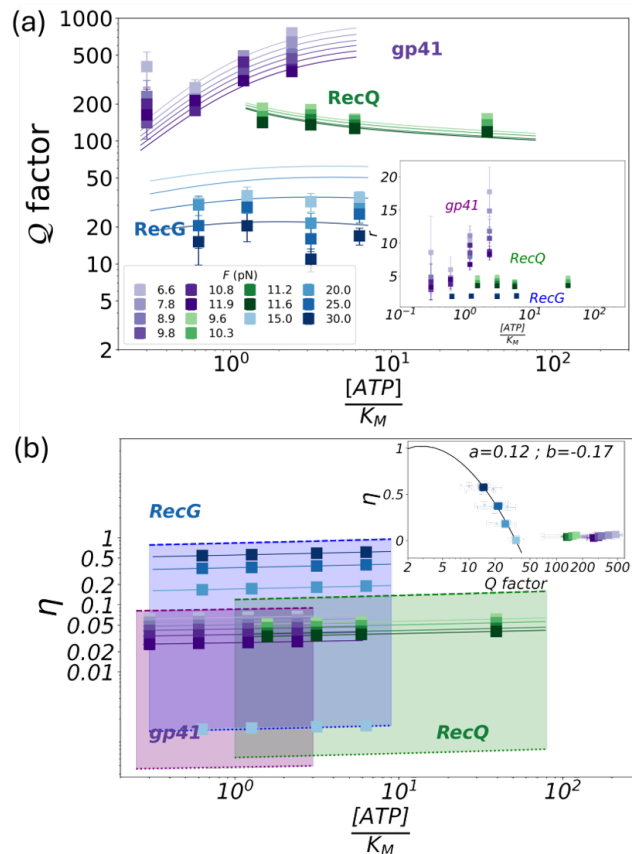

FIG. 5. (a) Estimated $\mathcal{Q}$ factor as a function of ATP concentration for different forces in a log-log scale for the three studied helicases, gp41 in purple, RecQ in green and RecG in blue. The ATP concentration is divided by the Michaelis-Menten constant of each helicase. Inset show the randomness parameter as a function of the ATP, the effect of pauses (b) Efficiency η as a function of the ATP concentration for different forces in a log-log scale. The inset shows η as a function of $\mathcal{Q}$ for the three helicases in a linear-log scale. The continuous line shows the fit to the RecG data of the function $\eta = 1 + a\log(\mathcal{Q}/2) + b\log^2(\mathcal{Q}/2)$.

IV.   DISCUSSION AND CONCLUSIONS

DNA replication and repair are fundamental processes of life by which genetic information is preserved and transferred to the next generation. These processes require the action of helicases that use ATP hydrolysis to

13

move on DNA inducing the unwinding and rewinding of the double helix [1–4]. In this work, we use magnetic and optical traps to monitor the motion of different DNA helicases (gp41, RecQ and RecG), while they move along DNA under different forces and ATP concentrations (Fig. 1).

Helicase dynamics can be characterized by measuring the velocity when the enzyme catalyzes the unwinding or rewinding reaction and the velocity when it translocates along single DNA strand. As shown in previous work, analysing how these velocities vary with applied force and ATP concentration provides insight into the helicase mechano-chemical cycle [13, 25–28, 38, 39]. Here, we extend this analysis by measuring the helicase diffusivity, which allows us to better characterize the helicase dynamics (Fig. 3). We use a Continuous Time Random Walk (CTRW) model, depicted in Figure 2, to describe the helicase dynamics that includes forward and backward steps and pauses. Analytical expressions for the helicase velocity and diffusivity can be derived and used to fit the data, allowing us to infer the minimal number of kinetic states and transitions necessary to capture the observed dynamics for each helicase (Fig. 4). As shown in a recent work [66], an analysis of the first-passage-time distribution can also be used to extract forward and backward rates and pause kinetics of motors. However, the study of motor difussivity presented here also allows us to explore fundamental thermodynamic constraints using the $\mathcal{Q} \geq 2$ factor of the Thermodynamic Uncertainty Relation (TUR), which is related to the helicase efficiency.

Importantly, incorporating an off-pathway pause state into the CTRW model is essential to reproduce the experimental data for all three helicases studied. Models without pauses, such as the Poisson or Random Walk model, do not fit the data, raising the question of the biological role of pauses. Helicases work in coordination with other enzymes to perform their biological functions. The RecQ and RecG helicases work with single-stranded binding proteins and other accessory proteins in different DNA repair pathways. Gp41 operates as part of a large complex containing two polymerases and other proteins, known as replisome and responsible for replicating the genomic DNA in T4 bacteriophage. Previously, we have shown that when the gp41 helicase works together with the polymerase, the velocity of the helicase advance increases without pausing [59]. Therefore, pausing might be the strategy to control helicase activity. Without the accessory proteins needed to develop a specific biological function, such as replication and repair, pauses stall the helicase activity.

A general feature observed for all helicases is that force affects unwinding and rewinding activity but not the translocation activity along one strand of DNA (Fig.4 (a,e), white versus gray background). The main effect of force is to destabilize the DNA duplex in a helicase-dependent manner. For gp41, the velocity and diffusivity are very sensitive to the value of the applied force, whereas for RecQ and RecG, they are not. Indeed, when the force changes by 5 pN, the velocity and diffusivity change by a factor of ten for gp41, whereas they remain almost constant for RecQ and RecG (Fig.4 a,c,e). This force sensitivity is related to their active and passive character, as discussed elsewhere [13].

Assuming a tight mechano-chemical coupling and using the diffusivity measurements we estimate the thermodynamic uncertainty factor $\mathcal{Q}$ and the efficiency η. RecG presents the smallest $\mathcal{Q}$ factor and largest efficiency as compared to gp41 and RecQ (Fig.5). In particular, at forces close to the stalling force ~ 40 pN, RecG reaches $\eta \sim 1$ by operating close to the thermodynamic optimization limit, $\mathcal{Q} = 2$. This large efficiency correlates with its large step-size of 3 bp. In contrast, gp41 and RecQ, which unwind only one bp per ATP hydrolysed, present much lower η, below 0.15. Remarkably, only RecG during rewinding shows efficiencies approaching 1, whereas unwinding activity for gp41 and RecQ helicases is thermodynamic inefficient, with most of the energy from ATP hydrolysis released as heat. This fact indicates that the efficiency of molecular machines is largest whenever they operate uphill in the sense that the energy cost of the task W is comparable to the chemical energy from ATP hydrolysis, $\Delta\mu$. A similar phenomenon occurs for F1 Fo ATPase [82], which is almost 100% efficient when transporting protons against the electrochemical potential gradient to synthesize ATP. In contrast, in the presence of thermogenic proteins, ATP synthase decouples from the proton gradient, and the proton flow is employed to produce heat.

The CTRW framework proposed in this work allow to characterize helicase dynamics through velocity and diffusivity measurements, which can be directly obtained from single-molecule assays. The model proposed can be adapted to describe different types of molecular motors that move along DNA or through other templates, such as polymerases or kinesins, and it can be easily extended to motors that have variable step-sizes, or multiple pause states.

V. ACKNOWLEDGEMENTS

VI. CONFLICT OF INTEREST STATEMENT

None declared.

[1] Timothy M Lohman and Keith P Bjornson. Mechanisms of helicase-catalyzed dna unwinding. Annual review of biochemistry, 65(1):169–214, 1996.

[2] Narendra Tuteja and Renu Tuteja. Unraveling dna helicases: motif, structure, mechanism and function. European Journal of Biochemistry, 271(10):1849–1863, 2004.

[3] Emmanuelle Delagoutte and Peter H Von Hippel. Helicase mechanisms and the coupling of helicases within macromolecular machines part ii: Integration of helicases into cellular processes. Quarterly reviews of biophysics, 36(1):1–69, 2003.

[4] Anna Marie Pyle. Translocation and unwinding mechanisms of rna and dna helicases. Annu. Rev. Biophys., 37(1):317–336, 2008.

[5] Jonathan M Caruthers and David B McKay. Helicase structure and mechanism. Current opinion in structural biology, 12(1):123–133, 2002.

[6] Martin R Singleton, Mark S Dillingham, and Dale B Wigley. Structure and mechanism of helicases and nucleic acid translocases. Annu. Rev. Biochem., 76(1):23–50, 2007.

[7] Carlos Bustamante, Jan Liphardt, and Felix Ritort. The nonequilibrium thermodynamics of small systems. Physics today, 58(7):43–48, 2005.

[8] Emmanuelle Delagoutte and Peter H Von Hippel. Helicase mechanisms and the coupling of helicases within macromolecular machines part i: structures and properties of isolated helicases. Quarterly reviews of biophysics, 35(4):431–478, 2002.

[9] Smita S Patel and Ilker Donmez. Mechanisms of helicases. Journal of Biological Chemistry, 281(27):18265–18268, 2006.

[10] Juan MR Parrondo and Pep Español. Criticism of feynman's analysis of the ratchet as an engine. American Journal of Physics, 64(9):1125–1129, 1996.

[11] Wonmuk Hwang and Martin Karplus. Structural basis for power stroke vs. brownian ratchet mechanisms of motor proteins. Proceedings of the National Academy of Sciences, 116(40):19777–19785, 2019.

[12] Eric A Galburt and Eric J Tomko. Conformational selection and induced fit as a useful framework for molecular motor mechanisms. Biophysical chemistry, 223:11–16, 2017.

[13] M. Manosas, X. G. Xi, D. Bensimon, and V. Croquette. Active and passive mechanisms of helicases. Nucleic Acids Research, 38(16):5518–5526, 2010.

[14] SW Matson, S Tabor, and CC Richardson. The gene 4 protein of bacteriophage t7. characterization of helicase activity. Journal of Biological Chemistry, 258(22):14017–14024, 1983.

[15] Kevin D Raney, Lawrence C Sowers, David P Millar, and Stephen J Benkovic. A fluorescence-based assay for monitoring helicase activity. Proceedings of the National Academy of Sciences, 91(14):6644–6648, 1994.

[16] Jeong-Hoon Kim and Yeon-Soo Seo. In vitro assays for studying helicase activities. DNA Replication: Methods and Protocols, pages 361–379, 2009.

[17] Keir C Neuman and Attila Nagy. Single-molecule force spectroscopy: optical tweezers, magnetic tweezers and atomic force microscopy. Nature methods, 5(6):491–505, 2008.

[18] Chirlmin Joo, Hamza Balci, Yuji Ishitsuka, Chittanon Buranachai, and Taekjip Ha. Advances in single-molecule fluorescence methods for molecular biology. Annu. Rev. Biochem., 77(1):51–76, 2008.

[19] Jaya G Yodh, Michael Schlierf, and Taekjip Ha. Insight into helicase mechanism and function revealed through single-molecule approaches. Quarterly reviews of biophysics, 43(2):185–217, 2010.

[20] Wei Cheng, Sophie Dumont, Ignacio Tinoco Jr, and Carlos Bustamante. Ns3 helicase actively separates rna strands and senses sequence barriers ahead of the opening fork. Proceedings of the National Academy of Sciences, 104(35):13954–13959, 2007.

[21] Silvia Hormeno, Oliver J Wilkinson, Clara Aicart-Ramos, Sahiti Kuppa, Edwin Antony, Mark S Dillingham, and Fernando Moreno-Herrero. Human helb is a processive motor protein that catalyzes rpa clearance from single-stranded dna. Proceedings of the National Academy of Sciences, 119(15):e2112376119, 2022.

[22] Jonathan M Craig, Andrew H Laszlo, Henry Brinkerhoff, Ian M Derrington, Matthew T Noakes, Ian C Nova, Benjamin I Tickman, Kenji Doering, Noah F de Leeuw, and Jens H Gundlach. Revealing dynamics of helicase translocation on single-stranded dna using high-resolution nanopore tweezers. Proceedings of the National Academy of Sciences, 114(45):11932–11937, 2017.

[23] Ignacio Tinoco Jr and Carlos Bustamante. The effect of force on thermodynamics and kinetics of single molecule reactions. Biophysical chemistry, 101:513–533, 2002.

[24] Sophie Dumont, Wei Cheng, Victor Serebrov, Rudolf K Beran, Ignacio Tinoco Jr, Anna Marie Pyle, and Carlos Bustamante. Rna translocation and unwinding mechanism of hcv ns3 helicase and its coordination by atp. Nature, 439(7072):105–108, 2006.

[25] Noah Ribeck, Daniel L Kaplan, Irina Bruck, and Omar A Saleh. Dnab helicase activity is modulated by dna geometry and force. Biophysical journal, 99(7):2170–2179, 2010.

[26] Maria Spies. Two steps forward, one step back: determining xpd helicase mechanism by single-molecule fluorescence and high-resolution optical tweezers. DNA repair, 20:58–70, 2014.

[27] Yeonee Seol, Gábor M Harami, Mihály Kovács, and Keir C Neuman. Homology sensing via non-linear amplification of sequence-dependent pausing by recq helicase. Elife, 8:e45909, 2019.

[28] Andrew H Laszlo, Jonathan M Craig, Momčilo Gavrilov, Ramreddy Tippana, Ian C Nova, Jesse R Huang, Hwanhee C Kim, Sarah J Abell, Mallory deCampos Stairiker, Jonathan W Mount, et al. Sequence-dependent mechanochemical coupling of helicase translocation and unwinding at single-nucleotide resolution. Proceedings of the National Academy of Sciences, 119(36):e2202489119, 2022.

[29] Anatoly B Kolomeisky and Michael E Fisher. Molecular motors: a theorist's perspective. Annu. Rev. Phys. Chem., 58(1):675–695, 2007.

[30] R Dean Astumian. Thermodynamics and kinetics of molecular motors. Biophysical journal, 98(11):2401–

15

2409, 2010.

[31] David Keller and Carlos Bustamante. The mechanochemistry of molecular motors. Biophysical journal, 78(2):541–556, 2000.

[32] Karel Svoboda, Partha P Mitra, and Steven M Block. Fluctuation analysis of motor protein movement and single enzyme kinetics. Proceedings of the National Academy of Sciences, 91(25):11782–11786, 1994.

[33] Keir C Neuman, Omar A Saleh, Timothee Lionnet, Giuseppe Lia, Jean-Francois Allemand, David Bensimon, and Vincent Croquette. Statistical determination of the step size of molecular motors. Journal of Physics: Condensed Matter, 17(47):S3811, 2005.

[34] Andre C Barato and Udo Seifert. Thermodynamic uncertainty relation for biomolecular processes. Physical review letters, 114(15):158101, 2015.

[35] Yonghyun Song and Changbong Hyeon. Thermodynamic uncertainty relation to assess biological processes. The Journal of Chemical Physics, 154(13), 2021.

[36] Patrick Pietzonka, Andre C Barato, and Udo Seifert. Universal bound on the efficiency of molecular motors. Journal of Statistical Mechanics: Theory and Experiment, 2016(12):124004, 2016.

[37] M Venkatesan, LL Silver, and NG Nossal. Bacteriophage t4 gene 41 protein, required for the synthesis of rna primers, is also a dna helicase. Journal of Biological Chemistry, 257(20):12426–12434, 1982.

[38] M. Manosas, S. K. Perumal, P. R. Bianco, F. Ritort, S. J. Benkovic, and V. Croquette. Recg and uvsw catalyse robust dna rewinding critical for stalled dna replication fork rescue. Nature Communications, 4(1):2368, 2013.

[39] Timothée Lionnet, Michelle M Spiering, Stephen J Benkovic, David Bensimon, and Vincent Croquette. Real-time observation of bacteriophage t4 gp41 helicase reveals an unwinding mechanism. Proceedings of the National Academy of Sciences, 104(50):19790–19795, 2007.

[40] Debjani Bagchi, Maria Manosas, Weiting Zhang, Kelly A Manthei, Samar Hodeib, Bertrand Ducos, James L Keck, and Vincent Croquette. Single molecule kinetics uncover roles for e. coli recq dna helicase domains and interaction with ssb. Nucleic acids research, 46(16):8500–8515, 2018.

[41] Keiko Umezu, Koji Nakayama, and Hiroaki Nakayama. Escherichia coli recq protein is a dna helicase. Proceedings of the National Academy of Sciences, 87(14):5363–5367, 1990.

[42] Peter McGlynn and Robert G Lloyd. Rescue of stalled replication forks by recg: simultaneous translocation on the leading and lagging strand templates supports an active dna unwinding model of fork reversal and holliday junction formation. Proceedings of the National Academy of Sciences, 98(15):8227–8234, 2001.

[43] Maria Manosas, Michelle M Spiering, Zhihao Zhuang, Stephen J Benkovic, and Vincent Croquette. Coupling dna unwinding activity with primer synthesis in the bacteriophage t4 primosome. Nature chemical biology, 5(12):904–912, 2009.

[44] Ann M Valentine, Faoud T Ishmael, Vincent K Shier, and Stephen J Benkovic. A zinc ribbon protein in dna replication: primer synthesis and macromolecular interactions by the bacteriophage t4 primase. Biochemistry, 40(50):15074–15085, 2001.

[45] Douglas A Bernstein and James L Keck. Domain mapping of escherichia coli recq defines the roles of conserved n-and c-terminal regions in the recq family. Nucleic acids research, 31(11):2778–2785, 2003.

[46] Stephen L Slocum, Jackson A Buss, Yuji Kimura, and Piero R Bianco. Characterization of the atpase activity of the escherichia coli recg protein reveals that the preferred cofactor is negatively supercoiled dna. Journal of molecular biology, 367(3):647–664, 2007.

[47] Charlie Gosse and Vincent Croquette. Magnetic tweezers: micromanipulation and force measurement at the molecular level. Biophysical journal, 82(6):3314–3329, 2002.

[48] Timothée Lionnet, Jean-François Allemand, Andrey Revyakin, Terence R Strick, Omar A Saleh, David Bensimon, and Vincent Croquette. Single-molecule studies using magnetic traps. Cold Spring Harbor Protocols, 2012(1):pdb–top067488, 2012.

[49] Steven B Smith, Yujia Cui, and Carlos Bustamante. [7] optical-trap force transducer that operates by direct measurement of light momentum. In Methods in enzymology, volume 361, pages 134–162. Elsevier, 2003.

[50] Xiang Feng, Michelle M Spiering, Ruda de Luna Almeida Santos, Stephen J Benkovic, and Huilin Li. Structural basis of the t4 bacteriophage primosome assembly and primer synthesis. Nature communications, 14(1):4396, 2023.

[51] Wanli Wang, Eli Barkai, and Stanislav Burov. Large deviations for continuous time random walks. Entropy, 22(6):697, 2020.

[52] Ryszard Kutner and Jaume Masoliver. The continuous time random walk, still trendy: fifty-year history, state of art and outlook. The European Physical Journal B, 90:1–13, 2017.

[53] Elliott W Montroll and George H Weiss. Random walks on lattices. ii. Journal of Mathematical Physics, 6(2):167–181, 1965.

[54] Xavier Viader-Godoy, CR Pulido, Borja Ibarra, M Manosas, and F Ritort. Cooperativity-dependent folding of single-stranded dna. Physical Review X, 11(3):031037, 2021.

[55] Charles Truong, Laurent Oudre, and Nicolas Vayatis. Selective review of offline change point detection methods. Signal Processing, 167:107299, 2020.

[56] Martin R Singleton, Sarah Scaife, and Dale B Wigley. Structural analysis of dna replication fork reversal by recg. Cell, 107(1):79–89, 2001.

[57] Gábor M Harami, Yeonee Seol, Junghoon In, Veronika Ferencziová, Máté Martina, Máté Gyimesi, Kata Sarlós, Zoltán J Kovács, Nikolett T Nagy, Yuze Sun, et al. Shuttling along dna and directed processing of d-loops by recq helicase support quality control of homologous recombination. Proceedings of the National Academy of Sciences, 114(4):E466–E475, 2017.

[58] Jonathan M Craig, Maria Mills, Hwanhee C Kim, Jesse R Huang, Sarah J Abell, Jonathan W Mount, Jens H Gundlach, Keir C Neuman, and Andrew H Laszlo. Nanopore tweezers measurements of recq conformational changes reveal the energy landscape of helicase motion. Nucleic Acids Research, 50(18):10601–10613, 2022.

[59] Maria Manosas, Michelle M Spiering, Fangyuan Ding, Vincent Croquette, and Stephen J Benkovic. Collaborative coupling between polymerase and helicase for leading-strand synthesis. Nucleic acids research, 40(13):6187–6198, 2012.

[60] Michael Schlierf, Ganggang Wang, Xiaojiang S Chen, and Taekjip Ha. Hexameric helicase g40p unwinds dna in single base pair steps. Elife, 8:e42001, 2019.

[61] Bo Sun, Daniel S Johnson, Gayatri Patel, Benjamin Y Smith, Manjula Pandey, Smita S Patel, and Michelle D Wang. Atp-induced helicase slippage reveals highly coordinated subunits. Nature, 478(7367):132–135, 2011.

[62] George I Bell. Models for the specific adhesion of cells to cells: a theoretical framework for adhesion mediated by reversible bonds between cell surface molecules. Science, 200(4342):618–627, 1978.

[63] Leonor Michaelis, Maud L Menten, et al. Die kinetik der invertinwirkung. Biochem. z, 49(333-369):352, 1913.

[64] Hirotugu Akaike. A new look at the statistical model identification. IEEE transactions on automatic control, 19(6):716–723, 1974.

[65] Gideon Schwarz. Estimating the dimension of a model. The annals of statistics, pages 461–464, 1978.

[66] Daniel R Burnham, Hazal B Kose, Rebecca B Hoyle, and Hasan Yardimci. The mechanism of dna unwinding by the eukaryotic replicative helicase. Nature communications, 10(1):2159, 2019.

[67] Janid A Ali and Timothy M Lohman. Kinetic measurement of the step size of dna unwinding by escherichia coli uvrd helicase. Science, 275(5298):377–380, 1997.

[68] Markus G Rudolph and Dagmar Klostermeier. When core competence is not enough: functional interplay of the dead-box helicase core with ancillary domains and auxiliary factors in rna binding and unwinding. Biological chemistry, 396(8):849–865, 2015.

[69] Bettina Theissen, Anne R Karow, Jürgen Köhler, Airat Gubaev, and Dagmar Klostermeier. Cooperative binding of atp and rna induces a closed conformation in a dead box rna helicase. Proceedings of the National Academy of Sciences, 105(2):548–553, 2008.

[70] Manjula Pandey and Smita S Patel. Helicase and polymerase move together close to the fork junction and copy dna in one-nucleotide steps. Cell reports, 6(6):1129–1138, 2014.

[71] Kata Sarlós, Máté Gyimesi, and Mihály Kovács. Recq helicase translocates along single-stranded dna with a moderate processivity and tight mechanochemical coupling. Proceedings of the National Academy of Sciences, 109(25):9804–9809, 2012.

[72] Maria M Martinez-Senac and Martin R Webb. Mechanism of translocation and kinetics of dna unwinding by the helicase recg. Biochemistry, 44(51):16967–16976, 2005.

[73] Christopher P Toseland, Ben Powell, and Martin R Webb. Atpase cycle and dna unwinding kinetics of recg helicase. PloS one, 7(6):e38270, 2012.

[74] Jian-Bing Ma, Ze Chen, Chun-Hua Xu, Xing-Yuan Huang, Qi Jia, Zhen-Yu Zou, Chen-Yang Mi, Dong-Fei Ma, Ying Lu, Hui-Dong Zhang, et al. Dynamic structural insights into the molecular mechanism of dna unwinding by the bacteriophage t7 helicase. Nucleic Acids Research, 48(6):3156–3164, 2020.

[75] Patrick Pietzonka, Felix Ritort, and Udo Seifert. Finite-time generalization of the thermodynamic uncertainty relation. Physical Review E, 96(1):012101, 2017.

[76] Wonseok Hwang and Changbong Hyeon. Energetic costs, precision, and transport efficiency of molecular motors. The journal of physical chemistry letters, 9(3):513–520, 2018.

[77] Yonghyun Song and Changbong Hyeon. Thermodynamic cost, speed, fluctuations, and error reduction of biological copy machines. The journal of physical chemistry letters, 11(8):3136–3143, 2020.

[78] William D Piñeros and Tsvi Tlusty. Kinetic proofreading and the limits of thermodynamic uncertainty. Physical Review E, 101(2):022415, 2020.

[79] Ping Xie. Non-tight and tight chemomechanical couplings of biomolecular motors under hindering loads. Journal of theoretical biology, 490:110173, 2020.

[80] Josep M Huguet, Cristiano V Bizarro, Núria Forns, Steven B Smith, Carlos Bustamante, and Felix Ritort. Single-molecule derivation of salt dependent base-pair free energies in dna. Proceedings of the National Academy of Sciences, 107(35):15431–15436, 2010.

[81] Joshua W Shaevitz, Steven M Block, and Mark J Schnitzer. Statistical kinetics of macromolecular dynamics. Biophysical journal, 89(4):2277–2285, 2005.

[82] Ryohei Yasuda, Hiroyuki Noji, Kazuhiko Kinosita, and Masasuke Yoshida. F1-atpase is a highly efficient molecular motor that rotates with discrete 120 steps. Cell, 93(7):1117–1124, 1998.